Chinese Chemical Letters 37 (2026) 111947

Contents lists available at ScienceDirect

Chinese Chemical Letters

journal homepage: www.elsevier.com/locate/cclet

Enhanced structural coloration and thermal management *via* hydrophobic force-driven colloidal photonic crystals

Xiaoqing Yu[a,b,1], Jie Ren[a,1], Nianxiang Zhang[a], Zirong Li[b], Kebing Chen[a], Jiazhuang Guo[a], Su Chen[a,*], Guoxing Li[a,*], Chang Liu[a,*]

[a] State Key Laboratory of Materials-Oriented Chemical Engineering, College of Chemical Engineering, School of Energy Science and Engineering, Nanjing Tech University, Nanjing 210009, China
[b] College of Chemistry and Materials Engineering, Anhui Science and Technology University, Bengbu 233000, China

ARTICLE INFO

Article history:
Received 8 May 2025
Revised 1 October 2025
Accepted 12 October 2025
Available online 12 October 2025

Keywords:
Hydrophobic driving force
Colloidal photonic crystals
Structural color
Fiber scaffold
Passive daytime cooling

ABSTRACT

Developing passive cooling materials with dual functionality of high-performance thermal management and aesthetic appeal remains a critical challenge for sustainable development. Here, we present a hydrophobic force-driven assembly strategy to construct crack-free colloidal photonic crystals (CPCs) for colored passive daytime cooling (PDC) textiles. Monodispersed poly(styrene-hydroxypropyl acrylate-hexafluorobutyl methacrylate) (P(St-HPA-HFBMA)) colloidal particles with low surface energy (9 mN/m) and high monodispersity (PDI < 0.05) are synthesized *via* soap-free emulsion polymerization. The hexafluorobutyl terminal groups ($-C_3F_6$) enable robust hydrophobicity (water contact angle: 124°), facilitating crack-free CPC assembly through hydrophobic driving force. By integrating the CPCs with SiO_2 aerogel-embedded polyethylene oxide (PEO/SiO_2 aerogel) fiber scaffold based on microfluidic spinning technology, a colored hybrid composite film is fabricated, achieving 0.76 solar reflectance and 0.84 thermal emissivity in the atmospheric window (8-13 μm). Outdoor evaluations demonstrate a sub-ambient cooling temperature of 4.1 °C under 732 W/m² solar intensity, reaching the desirable level of PDC materials. The hybrid composite film also exhibits angle-independent structural colors, mechanical robustness (tensile strength: 1.86 MPa), and scalable manufacturability. This work provides a paradigm for multifunctional PDC systems combining aesthetic versatility with sustainable cooling performance.

© 2025 Published by Elsevier B.V. on behalf of Chinese Chemical Society and Institute of Materia Medica, Chinese Academy of Medical Sciences.

Thermal management has become more crucial to human life, from personal comfort to industrial production, and is intimately related to global sustainability. As an indispensable aspect, cooling mainly depends on the compression-based systems (air conditioners and refrigerators), which account for ~20 % of worldwide electricity consumption. And such cooling systems contribute significantly to the greenhouse effect through both energy-intensive operation and refrigerant leakage (hydrofluorocarbons) [1,2]. Therefore, it is urgent to develop alternative technologies for eco-friendly and energy-saving cooling. Passive daytime cooling (PDC), as a promising sustainable thermal management technology, has gained widespread attention. It is spontaneous heat dissipation within the atmospheric window (8-13 μm) and suppression of solar radiation (0.3-2.5 μm) based on high reflectivity, enabling effective cooling without any external electricity and coolant inputs [3–5]. Recent developments in photonic engineering have produced advanced PDC designs, including multilayer films [6], hybrid particle-matrix coatings [7], porous polymers [8], and even metamaterials [9]. Generally, most of these PDC designs tend to exhibit a white or metallic appearance, striving for high solar reflectivity. The glaring colors often cause light pollution and visual discomfort in practical applications. Besides, this limited color palette is a drawback in wearable applications, where visual aesthetics are key considerations [10,11]. Therefore, the PDC designs that can demonstrate the balance between high-performance cooling functionality and aesthetic versatility are highly meaningful and desirable.

Colloidal photonic crystals (CPCs) with periodically structured dielectric lattices exhibit unique photonic band gaps (PBGs) that enable wavelength-selective solar radiation modulation through Bragg diffraction [12,13]. Additionally, structural color derives from the PBGs of CPCs through light-matter interactions, offering an eco-friendly alternative to conventional absorption-based chromophores that suffer from photothermal heating in PDC appli-

* Corresponding authors.
E-mail addresses: chensu@njtech.edu.cn (S. Chen), xing1065172121@163.com (G. Li), liuchang09@njtech.edu.cn (C. Liu).
[1] These authors contributed equally to this work.

https://doi.org/10.1016/j.cclet.2025.111947
1001-8417/© 2025 Published by Elsevier B.V. on behalf of Chinese Chemical Society and Institute of Materia Medica, Chinese Academy of Medical Sciences.

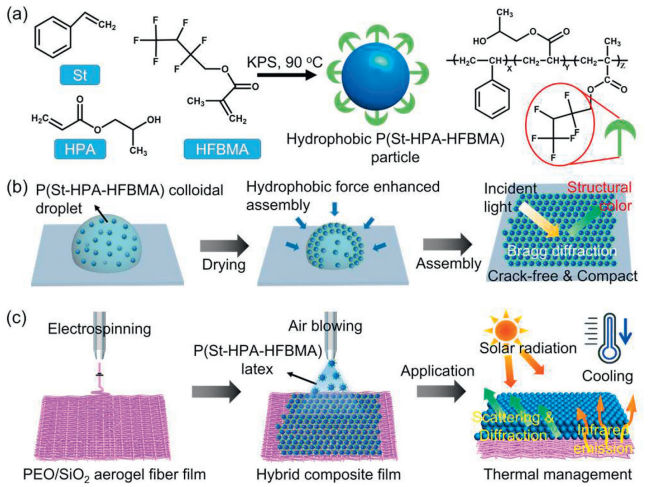


Fig. 1. (a) Schematic illustration of the synthesis of the hydrophobic P(St-HPA-HFBMA) monodispersed colloidal particles *via* emulsion polymerization. (b) Schematic representation of the assembly process of the P(St-HPA-HFBMA) particles. Hydrophobic force induces crack-free CPCs to appear brilliant structural color. (c) Illustration for the manufacture of colored hybrid composite film *via* microfluidic spinning strategy and their application in thermal management.

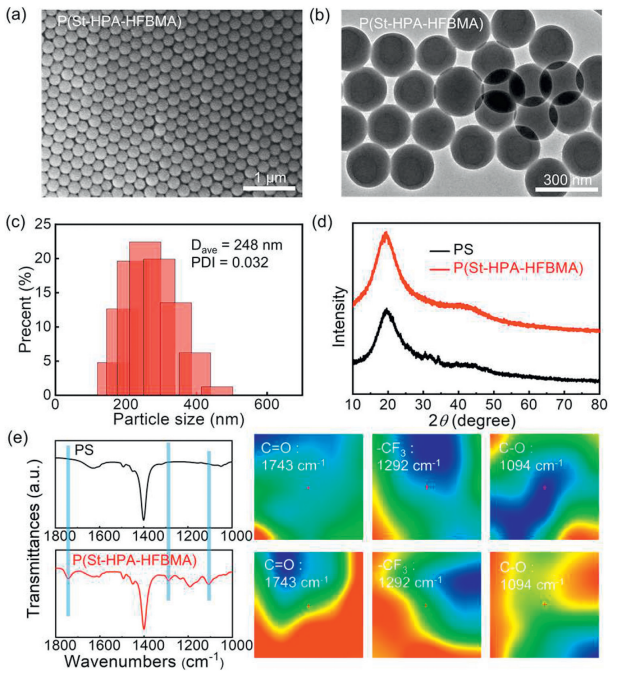


Fig. 2. (a) SEM image, (b) TEM image, and (c) particle size distribution for a typical P(St-HPA-HFBMA) monodispersed colloidal latex. (d) XRD patterns of P(St-HPA-HFBMA) and pure PS samples. (e) IR spectra of P(St-HPA-HFBMA) and PS particles, and the corresponding micro-IR images of characteristic peaks.

cations [14]. Obviously, CPCs demonstrate a groundbreaking solution for integrating spectral management with structural coloration through their periodic dielectric microstructures. Owing to that, CPCs have been served as colored cooling materials for daytime thermal management. In this regard, Ma's group introduced a structural color-based passive cooler, where interference-induced retroreflection in CPCs enables tunable chromaticity while maintaining high solar reflectance. The colored coolers achieved 4 °C sub-ambient cooling under 1000 W/m^2 solar radiation [15]. Chen and co-workers presented a colored textile for PDC by spraying ZnS@SiO_2 colloidal crystals on a polyethylene terephthalate textile. The colored textile could reduce the simulated skin temperature by ~6 °C under direct sunlight [16]. Moreover, our group designed Ag@CPC metamaterial coatings, demonstrating excellent daytime cooling performance with a theoretical cooling power of 30.4 W/m^2 [17]. Despite these promising developments, mainstream CPC building blocks, including polymethylmethacrylate (PMMA), polystyrene (PS), and silica (SiO_2) particles, usually suffer from low assembly efficiency, large-scale cracking morphology, and dim structural color because of the weak inter-particle interactions [18]. These limitations greatly restrict the practical application of CPCs. To solve these, shear-induced assembly strategy provides a high-efficient route for the construction of large-scale CPCs, in which shear forces promote the directional migration and rearrangement of colloidal particles [19,20]. Meanwhile, hydrophobic interactions at the molecular scale have been utilized to drive CPC assembly. Typically, Jiang and co-workers achieved crack-free CPCs with narrow PBGs based on the hydrophobic force from the substrate [21]. And our group proposed a hydrophobic force driving self-assembly strategy for large-scale and crack-free poly(*tert*-butylacrylate) CPCs [22]. This hydrophobic engineering approach enhances particle-particle and particle-substrate interactions, enabling crack-free photonic architectures with well-defined Bragg diffraction peaks. This advancement motivates the exploration of extra hydrophobic forces for facilitating high-quality CPCs with crack-free lattice and brilliant structural colors.

Herein, we develop poly(styrene-hydroxypropyl acrylate-hexafluorobutyl methacrylate) (P(St-HPA-HFBMA)) monodispersed colloidal particles with robust hydrophobicity (water contact angle: 124°) and highly monodispersity (polydispersity index (PDI) < 0.05) *via* the one-step emulsion polymerization (Fig. 1a). The hexafluorobutyl terminal groups (–C_3F_6) confer low surface energy (9 mN/m) to colloidal particles, enabling the assembled CPCs to show brilliant structural color, excellent hydrophobic properties, and large-scale crack-free morphology. This work establishes a proof-of-concept for hydrophobic force-driven assembly, wherein regulated interparticle interactions promote more efficient and ordered packing of colloidal particles (Fig. 1b). We further integrate the resultant P(St-HPA-HFBMA) CPCs with SiO_2 aerogel-embedded polyethylene oxide (PEO/SiO_2 aerogel) fiber scaffold based on the microfluidic spinning strategy, yielding a colored hybrid composite film tailored for colored PDC textiles. The resulting colored PDC textile establishes high reflectivity (0.76) to solar radiation, while its thermal emissivity (0.84) in the atmospheric window accelerates heat dissipation. Promisingly, an average 4.1 °C sub-ambient cooling temperature is achieved by the designed colored textile when exposed to sunlight with an average 732 W/m² solar intensity (Fig. 1c). Notably, the colored PDC textile also demonstrates superior flexibility, mechanical strength, and tailoring designability, highlighting their potential for practical applications. Hence, we firmly believe that this work would give reliable guidance for the construction of functional and high-quality CPCs and advance the development of multifunctional PDC systems that harmonize aesthetic versatility with sustainable cooling.

The construction of CPCs with large-scale and crack-free morphology and desirable optical properties starts from the synthesis of P(St-HPA-HFBMA) monodispersed colloidal particles *via* an easy-to-perform soap-free emulsion polymerization. The HFBMA monomer, which is characterized by hexafluorobutyl terminal groups (–C_3F_6), imparts exceptional hydrophobicity to the particles. This feature favors exerting hydrophobic driving force for the self-assembly of CPCs, and facilitates the formation of structurally ordered CPCs with vivid structural color and crack-free morphology [23,24]. As proof of concept, the microstructure of the P(St-HPA-HFBMA) CPCs was observed by the scanning electron microscope (SEM). As shown in Fig. 2a, the uniform and hexagonally close-packed particle arrangements were displayed, indicating a long-

range ordered face-centered cubic (FCC) lattice. Transmission electron microscopy (TEM) further confirmed regular spherical morphologies and well-defined core/shell architecture of the P(St-HPA-HFBMA) particles (Fig. 2b). Moreover, we carried out dynamic light scattering (DLS) analysis to determine the size distribution of particles. The particle size distribution of the P(St-HPA-HFBMA) sample was centered at 248 nm with a PDI of 0.032 (below 0.05) (Fig. 2c). The merit of regular spherical morphologies and high monodispersity of the P(St-HPA-HFBMA) colloidal particles are favorable guarantees for high-quality CPC assembly.

Furthermore, X-ray diffraction (XRD) measurements were also performed to elucidate the structural evolution of particle assembly. The diffraction peak at $2\theta \approx 20°$ corresponds to the amorphous PS. Obviously, for the P(St-HPA-HFBMA) sample, the diffraction peak at $2\theta \approx 20°$ is sharper and more intense than that of the PS sample, which could be attributed to the enhanced crystallinity arising from the hydrophobic fluorinated side chains (Fig. 2d) [25]. Meanwhile, we conducted Fourier transform infrared (FT-IR) spectroscopy characterization to analyze the chemical compositions of PS and P(St-HPA-HFBMA) particles. The peaks at 1600, 1580, 1500, and 1450 cm^{-1} are assigned to aromatic C=C vibrations in PS. Along with the introduction of the P(HPA-HFBMA) shell, several new characteristic peaks could be observed. The peaks located at 1292, 840, and 1743 cm^{-1} are ascribed to $-CF_3$, $-CF_2-$, and C=O vibrations, respectively, indicating the existence of HFBMA units in the resultant particles. And the peak at 1094 cm^{-1} belongs to C–O stretching vibration, which illustrates the hydroxyl group of HPA units (Fig. S1 in Supporting information). Micro-IR images further highlighted intensified signals at 1743, 1292, and 1094 cm^{-1} in P(St-HPA-HFBMA) sample, contrasting with weaker intensities in PS sample (the red corresponds to high intensity while the blue encodes low intensity) (Fig. 2e). Therefore, these findings collectively validate the successful synthesis of P(St-HPA-HFBMA) particles. The particles enriched with hexafluorobutyl terminal groups establish hydrophobic driving forces to guide the self-assembly of CPCs. Besides, HFBMA contains fluorine atoms with strong electronegativity. It further attenuates molecular interactions, guaranteeing the P(St-HPA-HFBMA) particles with a relatively lower glass transition temperature ($T_g = 68$ °C). This feature also benefits the enhancement of self-assembly of CPCs (Fig. S2 in Supporting information) [26].

To systematically investigate the role of hydrophobicity in governing CPC structures and structural color, P(St-HPA-HFBMA) particles were synthesized with varying mass fractions of HFBMA monomers (0–40 wt%). Remarkably, colloidal particles kept desirable monodispersity (PDI < 0.05) across HFBMA concentration ranging from 0 to 30 wt%. However, when the HFBMA concentration increased to 40 wt%, the PDI of colloidal particles was changed into 0.072 due to microphase separation and secondary nucleation [26]. Generally, highly monodispersity (PDI < 0.05) is the fundamental guarantee for the construction of high-quality CPCs (Fig. S3 in Supporting information) [27]. As illustrated in the SEM images, the assembled CPC films exhibited progressively enhanced structural ordering with increasing HFBMA monomer concentration (0-30 wt%), transitioning from poorly ordered particle arrangement to well-defined FCC lattice with reduced interparticle spacing. In contrast, colloidal particles containing 40 wt% HFBMA monomers failed to assemble long-range ordered lattice structures (Fig. S4 in Supporting information), resulting in amorphous photon structure. As clearly indicated in Fig. S5 (Supporting information), the pure PS CPC film suffered from severe cracks and dim structural color on the macroscopic view. Whereas, as the increasing of HFBMA mass fraction (from 0 to 30 wt%), the crack degrees of CPC films were gradually suppressed, ultimately yielding crack-free films.

Meanwhile, the optical properties were obviously improved with the increasing hydrophobic monomers concentration. To quantify the photonic performance of CPCs, we analyzed both the normalized full width at half-maximum ($\Delta\lambda/\lambda_{max}$) and the ratio of the peak intensity to background ($I_{max}/I_{background}$) [28,29]. The $\Delta\lambda/\lambda_{max}$ reflects lattice structure in CPCs. The value of $\Delta\lambda/\lambda_{max}$ of CPC films gradually decreases as the increasing of HFBMA mass fraction (from 0 to 30 wt%), demonstrating the enhanced packing ordering. Correspondingly, the $I_{max}/I_{background}$ value raised from 8.5 for pure PS CPCs to 38 for P(St-HPA-HFBMA) CPCs (30 wt% HFBMA), ascribed to the highly ordered particle arrangement. However, excessive hydrophobic HFBMA monomers cannot guarantee monodispersity of resultant colloidal particles. And thus, the P(St-HPA-HFBMA) CPCs (40 wt% HFBMA) present disordered assembly structure and poor optical properties. Consequently, the $I_{max}/I_{background}$ value was significantly reduced and $\Delta\lambda/\lambda_{max}$ value simultaneously increased due to multiple incoherent scatterings (Fig. S6 in Supporting information). As expected, the static water contact angles of the corresponding CPC films increased from 86° to 115°, 120°, and 124°, respectively, showing enhanced hydrophobicity. Based on this, we can preliminarily conclude that the morphological evolution of CPC film correlated with enhanced hydrophobicity. Hexafluorobutyl groups provide driving forces for hydrophobic force-mediated particle assembly, thereby enabling CPCs with close-packed FCC lattices. Moreover, taken both hydrophobicity and assembly structure into consideration, the colloidal particles with 30 wt% HFBMA monomer fractions were chosen as the optimum sample for the follow-up experiments.

In terms of the assembly mechanism, we directly compared the assembly behavior of pure PS and P(St-HPA-HFBMA) (HFBMA mass fraction: 30 wt%) colloidal particles. It is worth noting that the resultant P(St-HPA-HFBMA) CPCs presented robust hydrophobicity (static water contact angle: 124°), large-scale crack-free morphology, and brilliant structural color. While the pure PS CPCs displayed severe cracks and dim color (Fig. 3a and Fig. S7 in Supporting information). Specifically, we can observe the P(St-HPA-HFBMA) CPCs exhibited a distinct diffraction peak with sharp spectral resolution, alongside a 4.47-fold enhancement in $I_{max}/I_{background}$ and 0.04 reduction in $\Delta\lambda/\lambda_{max}$ compared to pristine PS CPCs (Fig. 3b). These results further corroborate the highly ordered crystalline structure and bright structural color of the as-prepared P(St-HPA-HFBMA) CPCs. Real-time monitoring of the assembly process of pure PS and P(St-HPA-HFBMA) CPCs (initial particle concentration: 20 wt%) was demonstrated in Fig. 3c. The pure PS droplet left a deposit with obvious cracks and dim color upon drying. In contrast, the P(St-HPA-HFBMA) particles were found to effectively suppress the cracks, resulting in a crack-free morphology with more uniform and brighter structural color. It is very promising that the assembly efficiency of the P(St-HPA-HFBMA) CPCs demonstrated a 40 % enhancement compared to pure PS CPCs, prompting the postulation of a hydrophobicity force-driven assembly mechanism. In most cases, conventional PS CPC assembly predominantly relies on asymmetric solvent evaporation, where capillary pressure, tensile stress, and shear stress synergistically induce cracks during film formation [18,30]. Whereas, the hexafluorobutyl terminal groups ($-C_3F_6$) dominating in P(St-HPA-HFBMA) particles could provide low free surface energy and hydrophobic driving force. Surface free energy calculations for colloidal particles often employ the following state-equation-based model (Eq. 1) [22,31]:

$$cos\theta = 2 \times \sqrt{\sigma_s/\sigma_l} \times e^{-\beta(\sigma_l-\sigma_s)^2} - 1 \quad (1)$$

where $\theta = 124°$ (static water contact angle), σ_l is the free energy of solvent (water), equaling 72 mN/m. And $\beta = 1.247 \times 10^{-4}$. For P(St-HPA-HFBMA) particles, this model yields an ultralow surface free energy of 9 mN/m (σ_s), being far lower than the PS particles (29 mN/m). The low surface free energy of colloidal particles ensures efficient hydrophobic driving force. In the assembly process of P(St-HPA-HFBMA) CPCs, the hydrophobic driving force might propel col-

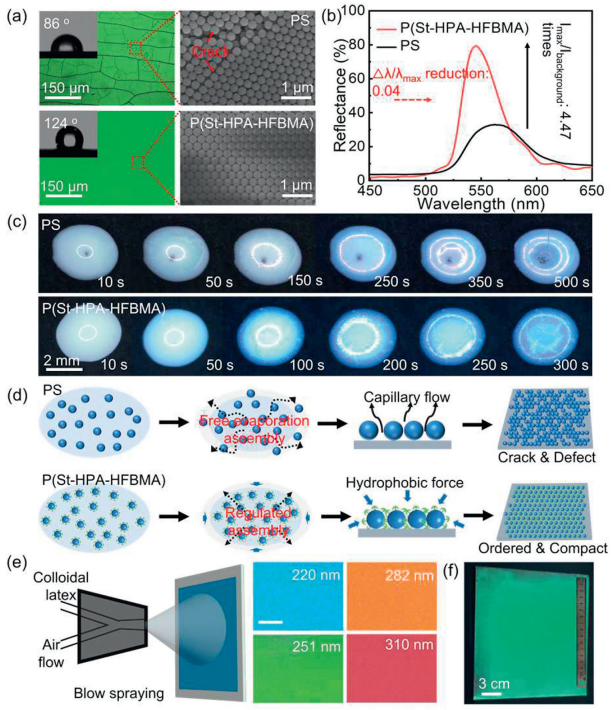


Fig. 3. (a) Optical photographs and SEM images of pure PS and P(St-HPA-HFBMA) CPCs. Insets: the static water contact angles of CPC films. (b) Reflection spectra confirm the enhanced optical properties of the P(St-HPA-HFBMA) CPCs compared to pure PS CPCs. (c) Real-time assembly of pure PS and P(St-HPA-HFBMA) CPCs on substrate. (d) Schematic illustration of the assembly of monodispersed colloidal particles towards CPCs. Hydrophobic P(St-HPA-HFBMA) particles tend to form ordered and compact arrangement, while cracks and defects present in pure PS CPCs. (e) Optical microscope images of blue, green, orange, and red CPC films composed of hydrophobic P(St-HPA-HFBMA) particles with sizes of 220, 251, 282, and 310 nm. Scale bar = 300 μm. The CPC films are constructed *via* blow spraying, and the schematic representation is shown on the left. (f) Photograph of the resulting large-scale CPC film.

loidal particles towards the outermost surface of the droplet, while the particles accumulate to form a close-packed arrangement. The hydrophobic force-driven assembly mechanism opens up a regulated assembly mode, where particles shrink to establish well-ordered FCC lattices, accompanied by the retraction of the gas-liquid interface. That allows the crack suppression and facilitates large-scale crack-free CPCs (Fig. 3d) [22,32,33]. Consequently, the P(St-HPA-HFBMA) CPCs share distinct advantages of enhanced assembly efficiency, crack-free structure, and bright structural color, which are desirable in practical applications.

More attractively, the P(St-HPA-HFBMA) particles were applied to the blow spraying technology for robust CPC films. Therefore, a series of CPC films with brilliantly blue, green, orange, and red structural colors were achieved by varying the sizes of P(St-HPA-HFBMA) particles (220, 251, 282, and 310 nm) (Fig. S8 in Supporting information and Fig. 3e). The corresponding reflection peaks were positioned at 470, 543, 601, and 635 nm, respectively. In particular, a linear correlation between the size of P(St-HPA-HFBMA) particles and PBG was noted, which is in good agreement with Bragg's law (Fig. S9 in Supporting information) [34]. Similar to the common CPC films, the P(St-HPA-HFBMA) CPCs subject to poor mechanical stability and adhesion failure due to insufficient interfacial interactions. To address this, waterborne polyurethane (PU) additive was employed to enhance the mechanical stability of CPC. PU chains containing plenty of ester and hydroxyl groups strengthen particle-to-particle and particle-to-substrate interactions through hydrogen bonding (Fig. S10a in Supporting information) [19,35]. Notably, the adhesion grade of CPC film already reaches 2 when the incorporation of PU exceeds 2 wt%, according to the ISO2409-1992 standard in cross hatch adhesion test (Fig. S10b in Supporting information). The results basically meet the application standards of coatings and verify the hydrogen-bonding mechanism [14]. However, massive PU (3 wt%) promotes cross-linked network formation that disrupts colloidal ordering of CPC [36,37]. As shown in Fig. S10b, the structure color of CPC film from original bright yellow becomes pale pink as the addition of PU increases from 0 wt% to 3 wt%. This can be attributed to the perturbation of ordered particle assembly by cross-linked PU network (Fig. S10c in Supporting information). Significantly, the effect of the addition of 2 wt% PU on the optical properties of CPC is negligible. Thus, robust CPC coating with bright structural color can be firmly constructed on substrates with the assistant of 2 wt% PU. Promisingly, we successfully fabricated large-scale CPC film with a size of over 20 cm × 20 cm on PET substrate with the assistance of hydrophobic force-driven assembly (Fig. 3f). The P(St-HPA-HFBMA) CPC films appear crack-free structure and bright structural color, thus providing a feasible strategy for large-scale and high-quality CPC preparation.

Encouragingly, the PBGs of CPCs selectively suppresses propagation of incident light at specific wavelengths. This feature favors the control of photon harvest for colored PDC designs [17,38]. Leveraging the tunable structural color of P(St-HPA-HFBMA) CPCs and their scalable film-forming capability, we engineered colored PDC textiles by spraying the P(St-HPA-HFBMA) CPCs onto PEO/SiO_2 aerogel fiber film. To improve the cooling performance of the designed colored PDC textiles, SiO_2 aerogel micro-powder was incorporated into the fiber matrix. The mesoporous architecture of SiO_2 aerogel amplifies backward Mie scattering due to refractive index contrast between SiO_2 skeleton ($n \approx 1.45$) and air cavities ($n = 1$), resulting in strong solar reflectance towards colored PDC textiles [39,40]. Concurrently, phonon-enhanced Fröhlich resonance in SiO_2 aerogel augments infrared (IR) emission in the atmospheric window (8-13 μm), facilitating efficient radiative heat dissipation (Fig. S11 in Supporting information) [9,41]. Fabrication procedure of the colored PDC textiles (hybrid composite film) is schematically presented in Fig. 4a. The hybrid composite film started from the electrospinning of a PEO/SiO_2 aerogel fiber, in which SiO_2 aerogel was basically incorporated into the PEO fiber (Fig. S12 in Supporting information). At this stage, the component of the PEO/SiO_2 aerogel fiber film depends on the mechanical and cooling performance evaluations. The photothermal characteristic of SiO_2 aerogel guarantees the PDC performance of the PEO/SiO_2 aerogel fiber film. While the tensile strength of the PEO/SiO_2 aerogel fiber film greatly reduced from 2.16 MPa to 0.91 MPa as the increase of SiO_2 aerogel content (from 5 wt% to 10 wt%), which could be attributed to the particle agglomeration caused by the excess introduction of SiO_2 aerogel [42]. Hence, considering the balance between the cooling and mechanical performance, the PEO/SiO_2 aerogel fiber film with 5 wt% SiO_2 aerogel content was selected for the following experiments (Figs. S13 and S14 in Supporting information). Meanwhile, the thickness of the PEO/SiO_2 aerogel fiber film was settled as ~71 μm (electrospinning time: 7 h), corresponding to the basically saturated thick-dependent cooling performance (Fig. S15 in Supporting information).

The next step involved the assembly of the P(St-HPA-HFBMA) particles onto the surface of the PEO/SiO_2 aerogel fiber scaffold *via* blow spraying, to form a CPC structure. The CPC layer establishes robust composite with the PEO/SiO_2 aerogel fiber film based on hydrogen bond-dominated interfacial adsorption and diffusion entanglement of flexible molecular chains (Fig. S16 in Supporting information) [43,44]. At this point, the hybrid composite film with functions of both PDC and colored aesthetics was obtained. Meanwhile, this cost-effective fabrication methodology demonstrates scalability potential. Obviously, the thickness of the CPC layer also was re-

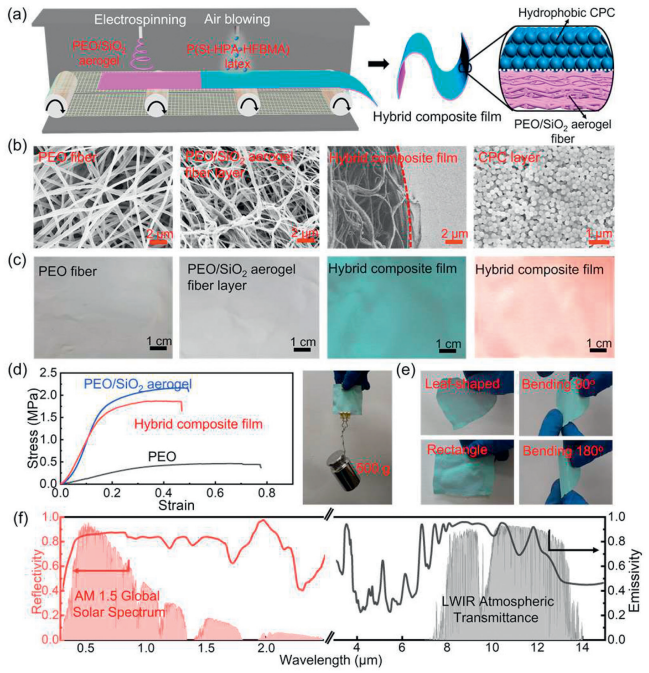


Fig. 4. (a) Illustration for the fabrication of the colored hybrid composite film *via* electrospinning and blow spaying strategies. (b) SEM images and (c) optical photographs of PEO fiber, PEO/SiO_2 aerogel fiber scaffold, and the hybrid composite film. (d) Stress-strain curves of PEO fiber, PEO/SiO_2 aerogel fiber scaffold, and the hybrid composite film. Inset: object lifting test of the hybrid composite film. (e) Digital photographs showing the hybrid composite film cutting into leaf and rectangle shapes, and suffering from bending. (f) Solar reflectance and thermal emittance of the hybrid composite film from 0.3 μm to 15 μm. The AM 1.5 global solar spectrum and the realistic atmospheric transmittance model are provided for reference.

sponsible for the structural color and cooling performance of the hybrid composite film. However, the hydrogen bond interactions between particles are unable to withstand external stress loads for thick CPC layer. The CPC layers with 40 min spraying time suffered from cracks. Thus, the desirable spraying time was determined to be 30 min corresponding to the CPC layer thickness of 15 μm (Fig. S17 in Supporting information).

The microstructures and morphologies of the fiber films were characterized by SEM, as presented in Figs. 4b and c. The pure PEO fiber film exhibited 3D interconnected microporous network structure, comprising randomly oriented nanofibers with a broad size distribution (centered at ~500 nm). The present phenomenon is quite general, we can notice that the incorporation of SiO_2 aerogel altered the fiber morphology. The PEO/SiO_2 aerogel fibers were much rougher and thicker compared to pristine PEO fibers. This special structure of the PEO/SiO_2 aerogel fiber film facilitates the strong broadband sunlight scattering, as evidenced by the white appearance. And P(St-HPA-HFBMA) particles were arranged on the nanofiber scaffold to build a long-range disordered, while short-range ordered photonic structure, yielding a colored hybrid composite film. By tuning the P(St-HPA-HFBMA) particle sizes to ~240 and ~280 nm, we successfully obtained green and orange hybrid composite films, respectively, demonstrating selective spectral control through Bragg diffraction engineering.

To verify the practical applicability of the hybrid composite films, mechanical strength and flexibility were discussed. The hybrid composite film can withstand a tensile stress of 1.86 MPa, which is slightly lower than the PEO/SiO_2 aerogel fiber film. Moreover, the hybrid composite film kept the capacity to sustain a 500 g load without structural failure and is sufficient for real-world usage (Fig. 4d). Additionally, as shown in Fig. 4e, the hybrid composite film presented superior tailoring designability, which can be easily cut into various shapes (rectangle and leaf shape). Furthermore, the hybrid composite film demonstrated the ability to withstand folding and rubbing. After repeated folding and rubbing, the color and configuration of the hybrid composite film still remained intact and firm. In addition, the film kept its original color at 90° and even 180° folding (Fig. S18 in Supporting information). The angle-independent color is ascribed to the amorphous photon structure [45], circumventing iridescence limitations in conventional applications. The reflection and emission characteristics of the colored hybrid composite film were quantified using ultraviolet-visible-near-infrared (UV-vis-NIR) and FT-IR spectroscopies equipped with integrating spheres (Fig. 4f). Notably, the hybrid composite film achieved 0.76 solar reflectance, which was attributed to the strong scattering effects of the plentiful pore distribution in the fiber structure and the optical gain of SiO_2 aerogel. Moreover, the P(St-HPA-HFBMA) CPCs can selectively reject the visible radiation based on Bragg diffraction, and the scattering in the visible region was further enhanced. Besides, the hybrid composite film exhibited high thermal emissivity of 0.84 in the atmospheric window (8-13 μm). The molecular structure of the hybrid composite film was responsible for its high thermal emissivity, where multiple vibration modes of C–F, C–O, and Si–O overlap with the atmospheric window [46,47]. Based on the above discussion, the hybrid composite film offers non-iridescent structural color, desirable mechanical properties, enhanced solar reflectance, and superior thermal emissivity, positioning it as an ideal candidate for next-generation textiles requiring desirable visual artistry and energy-saving thermal management.

The engineered photonic microstructure of the hybrid composite film enables selective spectral filtering with high solar reflectance, where the photonic architecture minimizes solar absorption while maximizing diffuse reflection to mitigate surface thermal accumulation (Fig. 5a). Moreover, the hybrid composite film also provides a strong thermal emittance in the atmospheric window, enabling efficient thermal emission to the cold outer space. These dual-band spectral responses undoubtedly endow the hybrid composite film with outstanding PDC performance, achieving sub-ambient cooling without energy consumption. In this aspect, we evaluated the cooling performance of the hybrid composite film using a solar simulator and a custom-built experimental setup (Fig. S19 in Supporting information) [48,49]. For reference, the experimental setup without any sample was regarded as the control group. The corresponding test results under 1000 W/m^2 simulated solar intensity were displayed in Fig. 5b. The temperature of the samples rose dramatically when the solar radiation was applied, and then the temperature reached a relatively stable equilibrium after around 15 min. The temperature of the PEO sample was about 1.5 °C lower than that of the control sample. In addition, the PEO/SiO_2 aerogel fiber film sample brought 4.7 °C cooling temperature for the control group. More significantly, the hybrid composite film sample attained a cooling temperature of 6.5 °C, outperforming both pure PEO and PEO/SiO_2 aerogel fiber films. We also investigated the effect of the solar intensity on the cooling performance of the hybrid composite film sample. The temperature of the control sample showed a linear increase from 45.1 °C to 56.1 °C under variable solar intensity (from 600 W/m^2 to 1200 W/m^2), and the hybrid composite film played a more positive cooling part in the high solar intensity environment (Fig. 5c and Fig. S20 in Supporting information). This seems to indicate that the strong reflectance of the hybrid composite film prevents heat harvesting, highlighting the environmental adaptability for cooling applications.

As documented in research, the inherent variability and complexity of outdoor environments substantially influence the operational efficacy of PDC systems. To confirm the practical PDC performance of the hybrid composite film, outdoor cooling evaluations were conducted on the six-floor rooftop of a building in Nanjing,

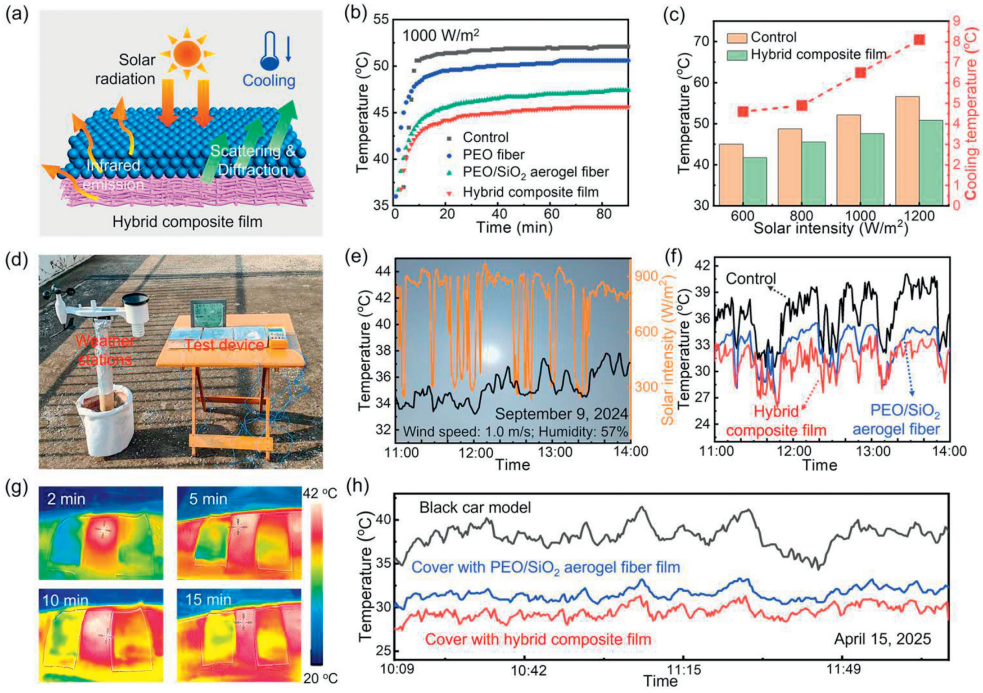


Fig. 5. (a) Schematic illustration of the hybrid composite film, designed for PDC *via* reflecting sunlight and emitting heat. (b) Real-time temperature of samples under 1000 W/m^2 simulated solar intensity. (c) Cooling performance evaluation dependent on the solar intensity for the hybrid composite film. (d) Photograph of the test device for daytime outdoor cooling measurement. (e) Recorded ambient parameters (solar intensity and ambient temperature) and (f) real-time temperature data of samples during daytime outdoor cooling measurement. (g) Infrared images of human skin covered with the colored hybrid composite film (left) and the PEO/SiO_2 aerogel fiber film (right) for personal thermal management. (h) Evaluation of the outdoor cooling performance of the colored hybrid composite film for car covers.

China (32°06′N, 118°40′E) under natural solar exposure (Fig. 5d) [50,51]. On September 9, 2024, the sample temperature, ambient parameter, and solar radiation were monitored continuously for 3 h from 11:00 to 14:00. The control sample exhibited minimal temperature deviation of 1.2 °C from ambient, validating the reliability and accuracy of the test method. As expected, an average 4.1 °C sub-ambient temperature was obtained for the hybrid composite film at midday with average solar irradiation of 732 W/m^2, and a maximum sub-ambient cooling temperature of 8.1 °C was reached. Notably, the cooling performance of the hybrid composite film was prioritized over the PEO/SiO_2 aerogel fiber sample (2.4 °C cooling temperature), and reached a higher level (Figs. 5e and f).

For practical application, the hybrid composite film was employed for personal thermal management, and its cooling performance was evaluated through *in vivo* human trials (human forearm skin) under 1000 W/m^2 simulated solar radiation. Infrared images revealed that bare skin maintained a steady-state temperature of ~40 °C. Whereas, the skin regions covered with the PEO/SiO_2 aerogel fiber sample showed a lower temperature than that of the exposed skin, indicating a good cooling effect. Remarkably, the hybrid composite film further enhanced this cooling effect for human skin, attributable to its photonic reflectance and radiative heat dissipation (Fig. 5g). The second set of experiments was concentrated on the cooling application of the colored hybrid composite film as car covers. An identical car model without the car cover was used as the control group, and the inner average temperature of the car model was up to 38.2 °C under the sky on April 15, 2025 (954 W/m^2 average solar intensity) (Fig. S21 in Supporting information). As illustrated, the colored hybrid composite film attained an average 8.7 °C cooling temperature for the car model (Fig. 5h). The hybrid composite films, coupled with the mechanical robustness and ease of fabrication, pose a versatile solution for large-scale PDC applications on the actual car or other large outdoor objects.

From the standpoint of daytime cooling applications, the operational stability of the designed hybrid composite film was evaluated. We firstly focused on the analysis for the stability of the hybrid composite film in high humidity atmospheres. The film can stand up to 70 % humidity without obvious mass and cooling performance loss, satisfying requirements for typical daytime operation (Fig. S22 in Supporting information). Additionally, 10-day accelerated aging test for the hybrid composite film was carried out under 1000 W/m^2 simulated solar radiation. The appearance of the film kept original green color and temperature also remained steady at ~45 °C (Fig. S23 in Supporting information). Furthermore, the hybrid composite film after accelerated aging was exposed under sunlight on June 26, 2025. Powerfully, the film still achieved an average 4.3 °C cooling temperature under average 667 W/m^2 solar radiation (Fig. S24 in Supporting information). Hence, the preeminent stability of the hybrid composite film constitutes both the core threshold for technological implementation and the critical bridge between experimental innovation and practical deployment.

In summary, we demonstrate a hydrophobic force-driven assembly strategy to fabricate large-area, crack-free CPCs for high-performance colored PDC textiles. The monodispersed P(St-HPA-HFBMA) particles, synthesized *via* soap-free emulsion polymerization, exhibit ultralow surface energy (9 mN/m) and exceptional hydrophobicity (124° water contact angle), enabling defect-free CPC assembly through regulated hydrophobic forces. The hydrophobic driving force suppresses crack formation by mitigating capillary stress during CPC assembly. And the blow spraying technique achieves 20 cm × 20 cm crack-free CPC films, demonstrating feasibility for real-world applications like architectural coatings or wearable devices. By integrating these CPCs with PEO/SiO_2 aerogel fiber scaffold, we engineer a hybrid composite film that synergistically combines angle-independent structural coloration (470-635 nm tunability), robust mechanical flexibility (1.86 MPa tensile strength, 180° folding durability), and dual-band optical optimization. The hybrid composite film offers 0.76 solar reflectance (enabled by CPC-selective reflection and PEO/SiO_2 aerogel fiber scattering) and 0.84 atmospheric window emissivity (from

SiO_2 phonon resonance), and excellent cooling performance of 4.1 °C sub-ambient temperature under 732 W/m² solar radiance is achieved. The hybrid composite film successfully addresses the long-standing trade-off between aesthetics and functionality in PDC materials. This work not only provides a paradigm for bridging aesthetic design with energy-saving cooling but also opens avenues for photonic materials in sustainable development and thermal management technologies.

Declaration of competing interest

The authors declare that they have no known competing financial interests or personal relationships that could have appeared to influence the work reported in this paper.

CRediT authorship contribution statement

Xiaoqing Yu: Writing – review & editing, Writing – original draft, Visualization, Validation, Methodology, Investigation, Formal analysis, Data curation, Conceptualization. **Jie Ren:** Writing – review & editing, Methodology, Investigation. **Nianxiang Zhang:** Writing – review & editing, Methodology, Formal analysis. **Zirong Li:** Software, Methodology, Investigation. **Kebing Chen:** Methodology, Formal analysis, Data curation. **Jiazhuang Guo:** Validation, Supervision, Project administration. **Su Chen:** Supervision, Project administration, Funding acquisition. **Guoxing Li:** Writing – review & editing, Supervision, Data curation. **Chang Liu:** Writing – review & editing, Validation, Supervision, Project administration, Funding acquisition, Conceptualization.

Acknowledgments

This work was supported by the National Natural Science Foundation of China (Nos. 22308160, 22278225, 22508184), the Natural Science Foundation of Jiangsu Province (Nos. BK20250610, BK20230327), Jiangsu Funding Program for Excellent Postdoctoral Talent (No. 2024ZB013), Postdoctoral Fellowship Program of CPSF (No. GZC20231112).

Supplementary materials

Supplementary material associated with this article can be found, in the online version, at doi:10.1016/j.cclet.2025.111947.

References

[1] X. Zhao, T. Li, H. Xie, et al., Science 382 (2023) 684–691.
[2] B. Li, Y. Kawakita, S. Ohira-Kawamura, et al., Nature 567 (2019) 506–510.
[3] J.P. Bijarniya, J. Sarkar, P. Maiti, Renew. Sust. Energ. Rev. 133 (2020) 110263.
[4] J. Li, Y. Jiang, J. Liu, et al., Nat. Sustain. 7 (2024) 786–795.
[5] M. Lee, G. Kim, Y. Jung, et al., Light: Sci. Appl. 12 (2023) 134.
[6] S. Jiang, M. Li, Z. Hu, et al., ACS Photonics 12 (2024) 528–536.
[7] W. Huang, Y. Chen, Y. Luo, et al., Adv. Funct. Mater. 31 (2021) 2010334.
[8] Y. Wang, X. Zhang, S. Liu, et al., Adv. Mater. 36 (2024) 2400102.
[9] Y. Zhai, Y. Ma, N.D. Sabrina, et al., Science 355 (2017) 1062–1066.
[10] T. Yu, R. Liu, Z. Yang, et al., Appl. Energ. 377 (2025) 124436.
[11] J. Zhao, F. Nan, L. Zhou, et al., Sol. Energ. Mat. Sol. C 251 (2023) 112136.
[12] J. Wu, X. Yu, G. Li, S. Chen, Chin. Chem. Lett. 35 (2024) 109234.
[13] Z. Cai, Z. Li, S. Ravaine, et al., Chem. Soc. Rev. 50 (2021) 5898–5951.
[14] W. Zhu, B. Droguet, Q. Shen, et al., Adv. Sci. 9 (2022) 2202061.
[15] S. Yu, Q. Zhang, Y. Wang, et al., Nano Lett. 22 (2022) 4925–4932.
[16] L. Du, R. Li, W. Chen, Chem. Eng. J. 475 (2023) 146431.
[17] X.Q. Yu, J. Wu, J.W. Wang, et al., Adv. Mater. 36 (2024) 2312879.
[18] A.Q. Xie, Q. Li, Y. Xi, et al., Acc. Mater. Res. 4 (2023) 403–415.
[19] Y. Wang, X. Li, Y. Zhang, et al., J. Mater. Chem. C 12 (2024) 254–261.
[20] H. Huang, H. Li, J. Yin, et al., Adv. Mater. 35 (2023) 2211117.
[21] Y. Huang, J. Zhou, B. Su, et al., J. Am. Chem. Soc. 134 (2012) 17053–17058.
[22] X. Wu, R. Hong, J. Meng, et al., Angew. Chem. Int. Ed. 58 (2019) 13556–13564.
[23] T.B. Chen, Q.N. Li, C. Liu, et al., Chem. Eng. J. 411 (2021) 128623.
[24] Y. Fang, P. Yan, Q. Zhang, X. Liu, Colloids Surfaces A 686 (2024) 133386.
[25] H. Xiang, X. Li, B. Wu, et al., Adv. Mater. 35 (2023) 2209581.
[26] X.Q. Yu, Z. Zhu, X. Wu, et al., Nanoscale 12 (2020) 19953–19962.
[27] Q. Chen, X. Ding, B. Yu, et al., Proc. Org. Coat. 137 (2019) 105287.
[28] M. Xiao, Z. Hu, Z. Wang, et al., Sci. Adv. 3 (2017) e1701151.
[29] J. Park, S. Kim, S. Magkiriadou, et al., Angew. Chem. Int. Ed. 53 (2014) 2899–2903.
[30] K.R. Phillips, C.T. Zhang, T. Yang, et al., Adv. Funct. Mater. 30 (2019) 1908242.
[31] J. Wang, C.F. Mbah, T. Przybilla, et al., ACS Nano 13 (2019) 9005–9015.
[32] Y. Tian, Z. Zhu, Q. Li, et al., Chem. Eng. J. 420 (2021) 127582.
[33] Y.T. Xu, J. Li, M.J. MacLachlan, Nanoscale Horiz. 7 (2022) 185–191.
[34] J. Fonseca, L. Meng, P. Moronta, et al., J. Am. Chem. Soc. 145 (2023) 20163–20168.
[35] Z. Zhu, J. Zhang, C. Wang, S. Chen, Macromol. Mater. Eng. 302 (2017) 1700013.
[36] B. Yi, H. Shen, J. Mater. Chem. C 5 (2017) 8194–8200.
[37] Y. Cui, F. Wang, J. Zhu, J. Colloid Interf. Sci. 531 (2018) 609–617.
[38] L. Yang, G. Wang, S. Duan, et al., ACS Appl. Mater. Interfaces 16 (2024) 62827–62837.
[39] W. Tang, Y. Zhan, J. Yang, et al., Adv. Mater. 36 (2024) 2310923.
[40] B. Ma, B. Wu, P. Hu, et al., J. Mater. Chem. A 11 (2023) 15227–15236.
[41] X.J. Kang, H. Zhang, C.Y. He, et al., Mater. Today Energy 43 (2024) 101579.
[42] H. Liu, L.Y. Lu, Y. Zhang, et al., Nanoscale 16 (2024) 12007–12012.
[43] Z. Li, W. Zheng, X. Ruan, et al., Chem. Eng. J. 495 (2024) 153578.
[44] J. Li, Z. Wang, L. Wen, et al., ACS Macro Lett. 5 (2016) 814–818.
[45] P. Xue, Y. Chen, Y. Xu, et al., Nano-Micro Lett. 15 (2022) 1.
[46] R. Liu, S. Wang, Z. Zhou, et al., Adv. Mater. 37 (2024) 2401577.
[47] J. Mandal, Y. Fu, A.C. Overvig, et al., Science 362 (2018) 315–319.
[48] P. Xu, B. Xiang, W. Zhong, et al., Sol. Energ. Mat. Sol. C 253 (2023) 112209.
[49] G.X. Li, T. Dong, L. Zhu, et al., Chem. Eng. J. 453 (2023) 139763.
[50] L. Zhou, X. Yin, Q. Gan, Nat. Sustain. 6 (2023) 1030–1032.
[51] T. Li, Y. Zhai, S. He, et al., Science 364 (2019) 760–763.